ACS OMEGA

http://pubs.acs.org/journal/acsodf

Article

Self-Assembled Hierarchical $Cu_xO@C_{18}H_{36}O_2$ Nanoflakes for Superior Fenton-like Catalysis over a Wide Range of pH

Ratul Rehman, Sudip Kumar Lahiri, Ashraful Islam, Peng Wei, and Yue Xu*

Cite This: *ACS Omega* 2021, 6, 22188–22201

Read Online

ACCESS | Metrics & More | Article Recommendations | Supporting Information

ABSTRACT: A novel copper-based catalyst supported by a long-chain hydrocarbon stearic acid ($Cu_xO@C_{18}H_{36}O_2$) was synthesized by a hydrothermal method and double replacement reactions. The as-prepared catalyst is shown as self-assembled hierarchical nanoflakes with an average size of ~22 nm and a specific surface area of 51.4 $m^2\ g^{-1}$. The catalyst has a good performance on adsorption as well as Fenton-like catalytic degradation of Rhodamine B (RhB). The catalyst (10 mg/L) showed an excellent adsorption efficiency toward RhB (20 mg/L) for pH ranging from 5 to 13, with the highest adsorption rate (99%) exhibited at pH 13. The Fenton-like catalytic degradation reaction of RhB (20 mg/L) by $Cu_xO@C_{18}H_{36}O_2$ nanoflakes was effective over a wide range of pH of 3−11, and $^{\bullet}OH$ radicals were generated via Cu_2O/H_2O_2 interactions in acidic conditions and CuO/H_2O_2 reactions in a neutral solution. The highest efficiency catalytic degradation of RhB (20 mg/L) was 99.2% under acidic conditions (pH = 3, H_2O_2 = 0.05 M), with an excellent reusability of 96% at the 6th cycle. The results demonstrated that the as-prepared $Cu_xO@C_{18}H_{36}O_2$ nanoflakes are an efficient candidate for wastewater treatment, with excellent adsorption capacity and superior Fenton-like catalytic efficiency and stability for RhB.

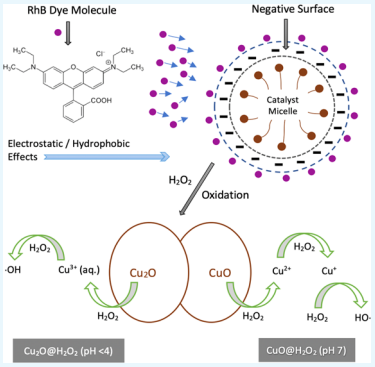

INTRODUCTION

With the rapid growth of human activities, the problem of water shortage is exacerbated by water contamination.[1] However, traditional industries, i.e., dyestuff, textile, and paper, unavoidably release a large number of dyes into water during the dyeing process of their products. Over 700 000 metric tons of dyestuffs and pigments are produced globally every year; meanwhile, nearly 10−15% of these dyes enter into water during production or processing, and 20% of these dyes are discharged directly into the environment as wastewater.[2] Among several organic pollutants present in dye wastewater, azo dyes have a highly stable aromatic structure with one or several azo bonds (−N═N−), making them difficult to degrade; Rhodamine B (RhB) is one of them.[3,4] There are various types of highly efficient water treatment technologies that came out recently.[5,6] Among the catalytic systems, the Fenton reaction is one of the most efficient advanced oxidation processes (AOPs) for azo dye degradation due to its nontoxic, eco-friendly, highly efficient, cost-effective, and sustainable oxidation.

The classical mechanism for the Fenton reaction is as follows

$$Fe(II) + H_2O_2 \rightarrow Fe(III) + HO^{\bullet} + HO^{-} \quad (1)$$

Fe(II) promotes hydrogen peroxide (H_2O_2) conversion to hydroxyl radical ($HO^{\bullet}$), and its chain reactions are involved in $HO^{\bullet}$ formation and decay in Fenton and Fenton-like structures.[7,8] Nevertheless, strong acidic reaction conditions, difficulties in nanoscale catalyst collections, and insufficient efficiency limit the application of traditional Fenton reactions.[9,10] Cocatalyst elements such as Cu, Sn, Ni, Fe, In, Ag, and other metals have been employed among all catalytic components studied.[11] Copper-based Fenton-like catalysts have received considerable attention.[12,13] Cu^{+} and Cu^{2+} are able to respond to H_2O_2 and have a wider range of pH due to the larger solubility constants of $Cu(OH)_2$.[14] Cu(I) as a "Fenton-like" catalyst acts as follows[15]

$$Cu(I) + H_2O_2 \rightarrow Cu(II) + HO^{\bullet} + HO^{-} \quad (2)$$

Further, Cu ions complexing with appropriate ligands could increase the stability and catalytic activity of copper-based catalysts. Incorporating the ligand in Cu^{2+} allows to electronically and sterically stabilize copper species and modulate the Cu^{+}/Cu^{2+} redox potential. Cu^{2+} complexes are theoretically effective activators in copper-catalyzed Fenton-like processes when coordinated with suitable ligands.[16,17]

In this work, stearic acid ($C_{18}H_{36}O_2$) was used as a complex ligand for an optimized copper-based Fenton-like nanocomposite catalyst and performed Fenton-like oxidation of azo dyes (RhB). Self-assembled hierarchical $Cu_xO@C_{18}H_{36}O_2$ nanoflake catalyst was synthesized by a hydrothermal method

Received: June 2, 2021
Accepted: August 4, 2021
Published: August 18, 2021

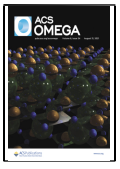

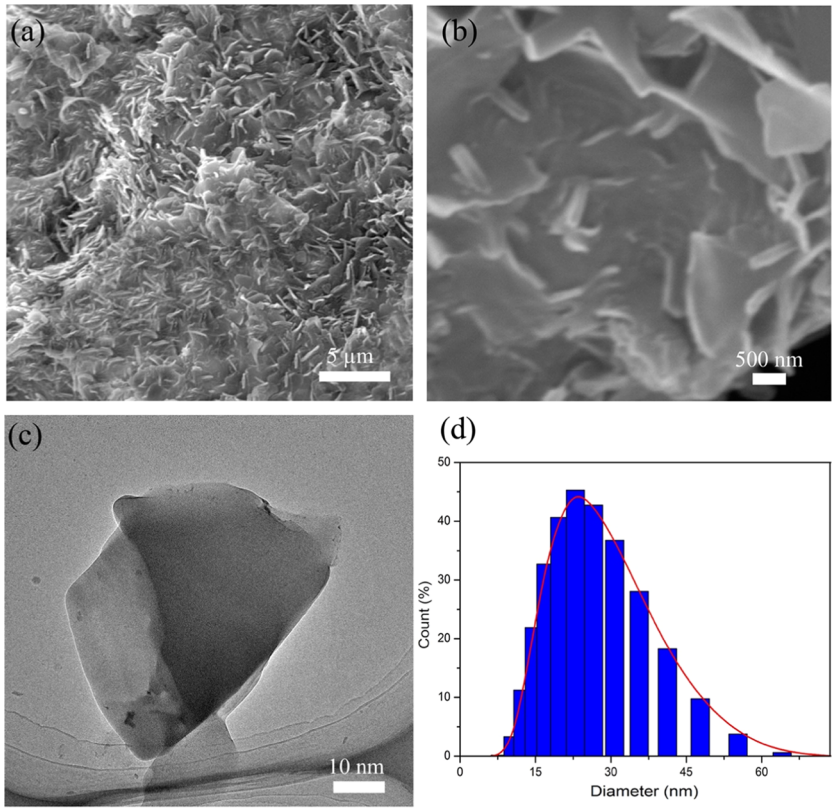

Figure 1. (a, b) Low-magnification and expanded FESEM images; (c) TEM image; and (d) size distribution histogram of the $Cu_xO@C_{18}H_{36}O_2$ catalyst.

and a double replacement reaction. The product exhibited a high adsorption efficiency of 99% in alkaline conditions, effective Fenton-like reaction catalytic degradation over a wide range of pH of 3−11, and high degradation reusability of 96% after six cycles. The fabrication process is well described and characterized through multiple techniques. The dye adsorption, adsorption kinetics, isotherm, desorption, and degradation were thoroughly investigated via controlling the time, pH, H_2O_2, and initial concentrations. Furthermore, the reusability was measured, and the proposed mechanism for adsorption and degradation has been illustrated.

RESULTS AND DISCUSSION

Structural Analysis and Chemical Properties. The catalyst was synthesized by the hydrothermal method and double replacement reaction. The coordination properties of copper (Cu) are similar to silver (Ag) in many cases, although copper is more prone to show Cu^{I}/Cu^{II} redox properties. Therefore, it is possible to prepare a Cu-containing metal−organic framework (MOF) while the structure remains similar to Ag. Copper oxides and their preparation are of concern to the researcher because of their economic price and environmental characteristics relating to precious transition-metal catalysts (platinum, silver, and gold).[18−20] However, it remains a challenge to develop a synthetic route that is safe and facile to operate. Stearic acid ($C_{18}H_{36}O_2$), as an excellent environmentally acceptable matrix for its biocompatibility and nontoxicity, is a saturated long-chain fatty acid derived from hydrolyzed animal or plant fat and contains a carboxyl group at one side and a methyl group toward the other end.[21] The polar head group of the stearic acid chain enables and facilitates binding with different metal cations and forms stable complexes. It is encouraged to use them widely as a support framework to stabilize various nanoparticles of metal/metal oxide. Moreover, the nonpolar tail group of stearic acid establishes strong attraction with various hydrophobic groups. To prevent agglomeration and enhance the size distribution of metal-oxide nanoparticles, various capping agents, including ethylenediamine (EDA),[22] poly(vinylpyrrolidone) (PVP),[23] and poly(allylamine) (PAAm),[24] are well known. Among them, PVP is widely used as a capping agent to enhance the nanoparticles' size and morphologies. PVP is a vinyl polymer with plain and strongly polar side groups owing to the peptide bond in the lactam chain.[25,26]

The morphology of the as-prepared $Cu_xO@C_{18}H_{36}O_2$ catalyst was characterized by a field-emission scanning electron microscope (FESEM) (Figure 1). It is shown in Figure 1a that the as-prepared sample exhibits a uniform, spherical, flowerlike nanoflake morphology all over the surface. These nanoflakes have rough surfaces and are composed of smaller nanoparticles. However, the high-magnification FESEM image (Figure 1b) indicates that the as-prepared $Cu_xO@C_{18}H_{36}O_2$ presents three-dimensional self-assembled hierarchical porous structures. Thus, the surface morphology changed and formed different sizes of nanoflakes on the surface after the double replacement reaction process of ion exchange between the sodium stearate and $CuSO_4{\cdot}5H_2O$. These structures are very suitable for producing excellent diffusion paths, thus enhancing the adsorption of molecules from the reaction system.[27] The hierarchical structure presents a high exposure area for dye adsorption site as well as the hydrophobic structure prevents acidic or alkaline solution reactions, resulting in the catalyst's excellent stability.[28] The transmission electron microscope (TEM) image shown in Figure 1c reveals that the random

https://doi.org/10.1021/acsomega.1c02881
ACS Omega 2021, 6, 22188−22201

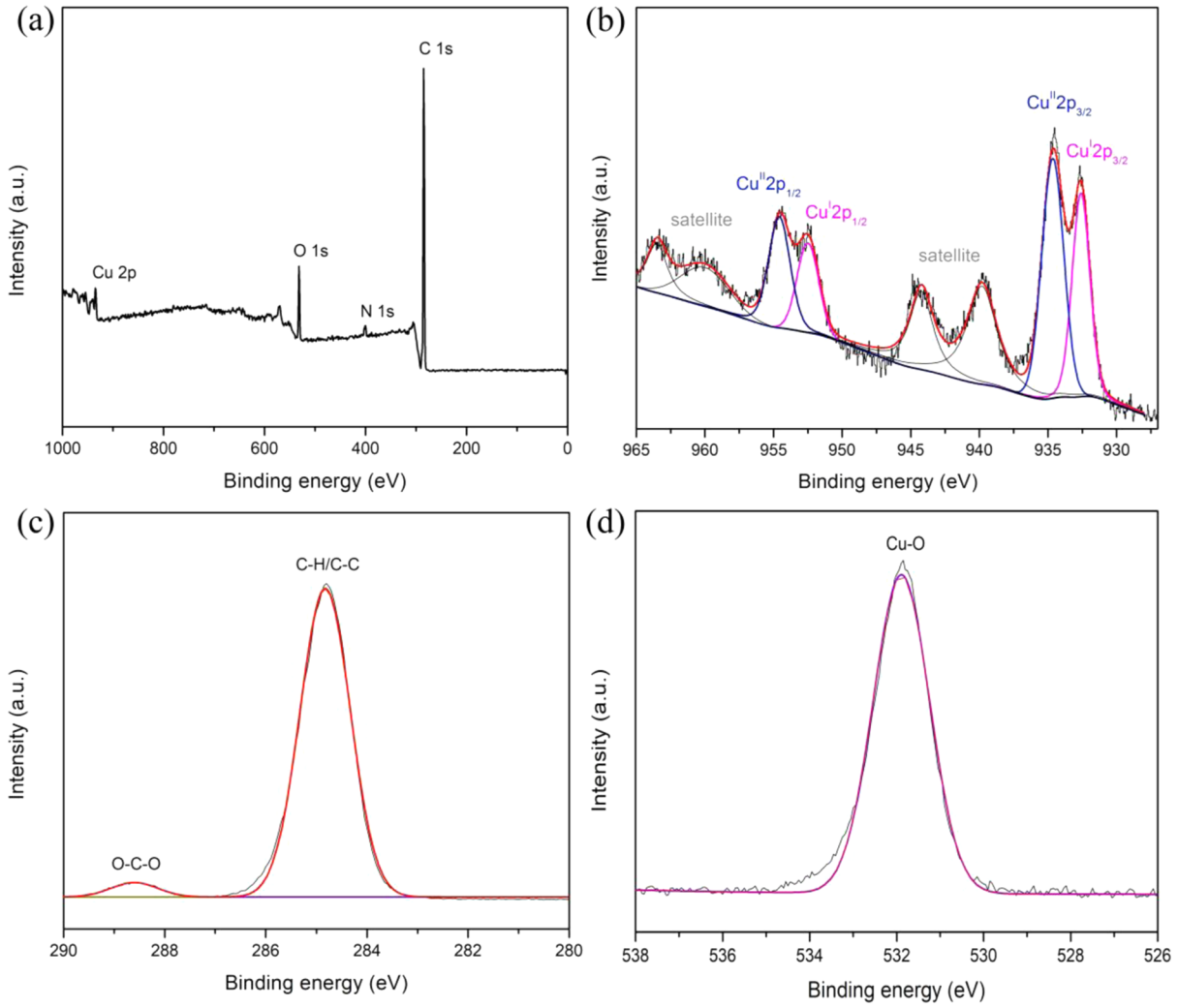

Figure 2. (a) XPS survey spectra of the $Cu_xO@C_{18}H_{36}O_2$ nanocomposite. High-resolution XPS core-level spectra of (b) Cu 2p, (c) C 1s, and (d) O 1s.

nanoflakes are loosely packed to each other without any distinct edge and continuous expansion. Moreover, the individual nanoflakes were formed simultaneously and coupled together. During the reaction, the copper ion was exchanged with sodium ion and formed stable complexes. As shown in Figure 1d, the average size of the nanocomposite was found to be 22.7 ± 4.0 nm, and no large particle was observed. The particles are single nanoflakes, implying a PVP-capped $Cu_xO@C_{18}H_{36}O_2$ nanocomposite.

As illustrated in Figure 2, the surface properties of nanoparticles were analyzed by X-ray photoelectron spectroscopy (XPS). The survey spectrum showed the presence of binding energy peaks of C, N, O, and Cu in Figure 2a. The N 1s peak at 399.8 eV can be assigned to the protonated amino groups.[29] The wide-scan spectra displayed two main peak positions at 934.5 and 954.6 eV, which were attributed to Cu $2p_{3/2}$ and Cu $2p_{1/2}$, respectively (Figure 2b). The high-resolution band of Cu $2p_{3/2}$ and $2p_{1/2}$ areas indicated Cu in monovalent and divalent oxidation states, and the peaks at 932.6 and 952.3 eV were assigned to the Cu_2O, while other peaks at 934.8 and 954.6 eV were the distinctive peaks of CuO.[30] It also recorded two "shake-up" satellite peaks positioned at 940 and 944.13 eV,[31] which appeared due to electron transfer from the ligand ($C_{18}H_{36}O_2$) orbital to the 3d orbital of Cu, confirming divalent Cu oxidation in the prepared samples.[32,33] The results of the XPS showed that the functional groups of amines (NH_2) and carbonyls (C═O) had suffered structural distortions in both shape and spectrum location, indicating their function in the complexation of Cu ions. The high resolution of Cu 2p core-level spectrum confirmed the formation of both Cu_2O and CuO. Regarding the C 1s core-level spectrum, as shown in Figure 2c, the binding peak at 284.8 eV was stimulated from the C−H or C−C bond, while the peak at 288.6 eV was assigned to O−C−O.[34] As shown in Figure 2d, for the O 1s spectrum, the peak at 532.0 eV was ascribed to the carboxyl oxygen (C═O) in the PVP repeated unit and correlated to the peroxo complexes (−O−O−) after copper oxide formation.[35]

Figure 3a presents the Fourier transform infrared spectroscopy (FT-IR) analysis of the $Cu_xO@C_{18}H_{36}O_2$ catalyst synthesized via ion exchange, and its functional groups are clarified. The presence of a small amount of PVP in the $Cu_xO@C_{18}H_{36}O_2$ catalyst is important since PVP can be a good stabilizer or capping agent.[36] From the FT-IR spectrum curves, the framework vibrations of the pyrrolidone ring observed at 1500 and 880 cm^{-1} correspond to the C═O stretching of the PVP polymer and the pyrrolidone ring slanted on the surface.[37,38] The peaks proved that the glycosidic linkage at 1082 and 1155 cm^{-1} are assigned to the aliphatic C−O bending and C−O stretching of the nanocomposite PVP polymer.[39] The peak around 1585 cm^{-1} belongs to the carbonyl stretch of stearic

https://doi.org/10.1021/acsomega.1c02881
ACS Omega 2021, 6, 22188−22201

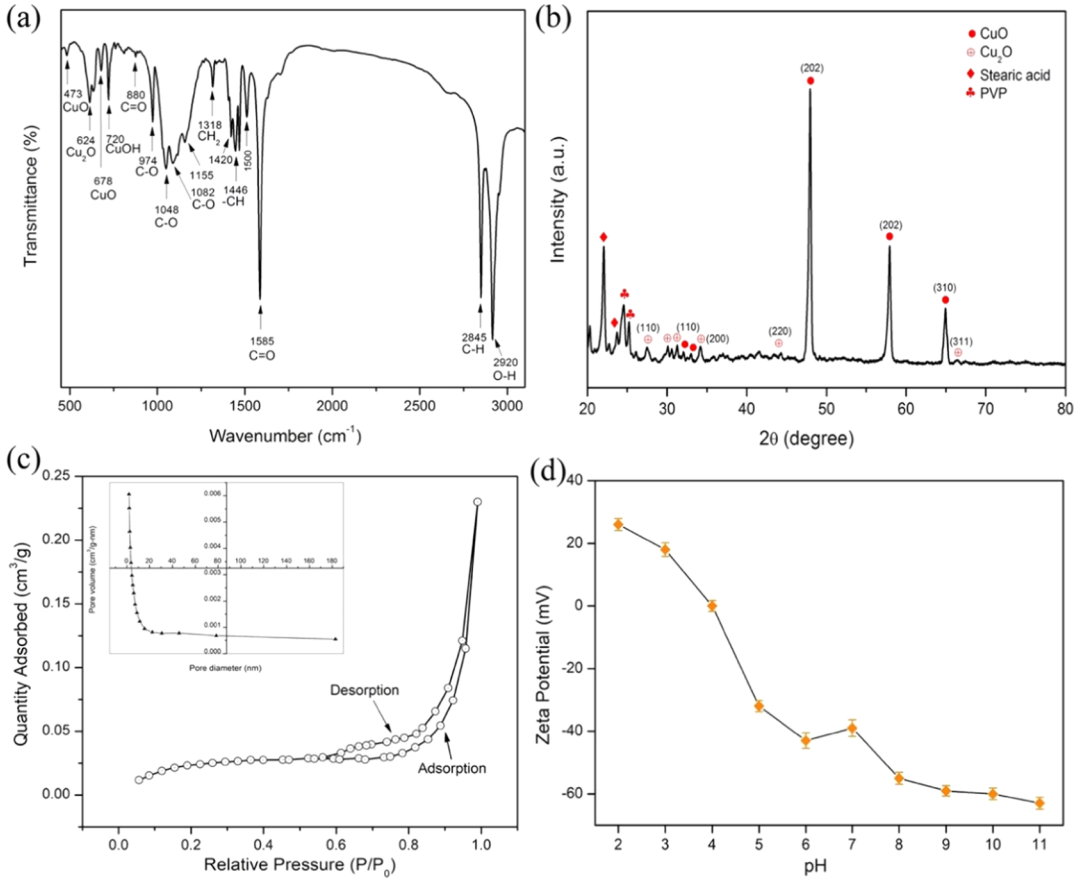

Figure 3. (a) FT-IR spectra. (b) XRD pattern of the as-synthesized $Cu_xO@C_{18}H_{36}O_2$ nanocomposite catalyst. (c) Nitrogen adsorption−desorption isotherms and (inset) the pore size distribution by the Barrett−Joyner−Halenda (BJH) adsorption. (d) ζ potentials of the synthesized catalyst.

acid.[40] The peaks of 2920 and 2845 cm^{-1} are assigned to the asymmetric C−H alkanes stretch and O−H carboxyl acid stretch, including the C−O stretch in amino acids identified at 1048 cm^{-1}.[41] FT-IR spectra suggest that the existence of the copper oxide nanoparticles is essential to prove the consistency of the oxide. The bands at 473 and 624 cm^{-1} are ascribed to CuO and Cu_2O vibrations, respectively.[42] The asymmetric and symmetric vibrations of the carboxylate group appeared at 1446 and 974 cm^{-1}, respectively. The plain peak at 678 cm^{-1} can be assigned to the stretching vibration of CuO, and the vibrational peak at 720 cm^{-1} is assigned to the Cu−O−H group active in CuO. The C−H bending and CH_2 wagging were reported at 1420 and 1318 cm^{-1}, respectively.[43] The above findings suggested that the sample contains several functional groups, including carboxyl and carbonyl groups.

The XRD patterns of the $Cu_xO@C_{18}H_{36}O_2$ catalyst support the existence of Cu_2O and CuO on the sample (shown in Figure 3b). The dominant diffraction peaks at 2θ = 32, 48, 58, and 65° corresponding to planes (110), $(20\bar{2})$, (202), and (310) have confirmed the presence of CuO (JCPDS No. 45-0937) and also clearly show small diffraction at 2θ values of 28, 32, 34, 43, and 66°, reflecting the lattice planes (110), (111), (200), (220), and (311) that have well associated with the Cu_2O structure (JCPDS No. 05-0667).[44] The reflection peaks at 22 and 23.8° are attributed to stearic acid with an intact crystalline structure.[45] Also, a couple of bands are located at 2θ = 22 and 24.56°, which may distinctly suggest the amorphous structure of the PVP.[46] This oxidation stability is most likely due to the presence of PVP, which is capped on the particles' surfaces. Cu ions are bound to the N or O atoms during the particle synthesis, as-synthesized copper particles are coated with absorbent PVP layers.[47]

The nitrogen adsorption and desorption isotherms, as well as the pore size distributions of the $Cu_xO@C_{18}H_{36}O_2$ catalyst, are depicted in Figure 3c. The Brunauer−Emmett−Teller (BET) formula was used to determine the specific surface area, and the Barrett−Joyner−Halenda (BJH) equation was used to calculate the average pore measurements using the adsorption isotherm branch. The curve corresponds to the presence of slit-shaped pores, where nitrogen occupies the gap between parallel plates. In both adsorption and desorption branches, the adsorption leap arises between partial pressures P/P_0 of 0.6−0.9. The increase in slope at about 0.6 leads to capillary condensation, which reveals the existence of mesopores and micropores;[48] however, higher relative pressures imply several interparticle porosities. The specific surface area of the sample was found to be 51.4 $m^2\ g^{-1}$, and the average uniform pore diameter was 11.5 nm (Figure 3c inset). The obtained results revealed that the nanocomposite exhibits a type (IV) isotherm with H3 hysteresis loops.[49]

The ζ-potential is associated with the electrophoresis stability of the particles in solution. The stability of a suspension is strongly linked with the ζ potential. The ζ-potential curves of the $Cu_xO@C_{18}H_{36}O_2$ nanocomposite are shown in Figure 3d. Here, the ζ potential decreases while the pH value increases, and above pH value 4, it changes to negative, which shows that sufficient acidic sites are available on the composite.[50] Moreover, RhB dye is categorized by its cationic nature, which increases its adsorption capability on the catalytic surface, thus resulting in good catalytic activity.[51] About the range of pH 5−11, the

https://doi.org/10.1021/acsomega.1c02881
ACS Omega 2021, 6, 22188−22201

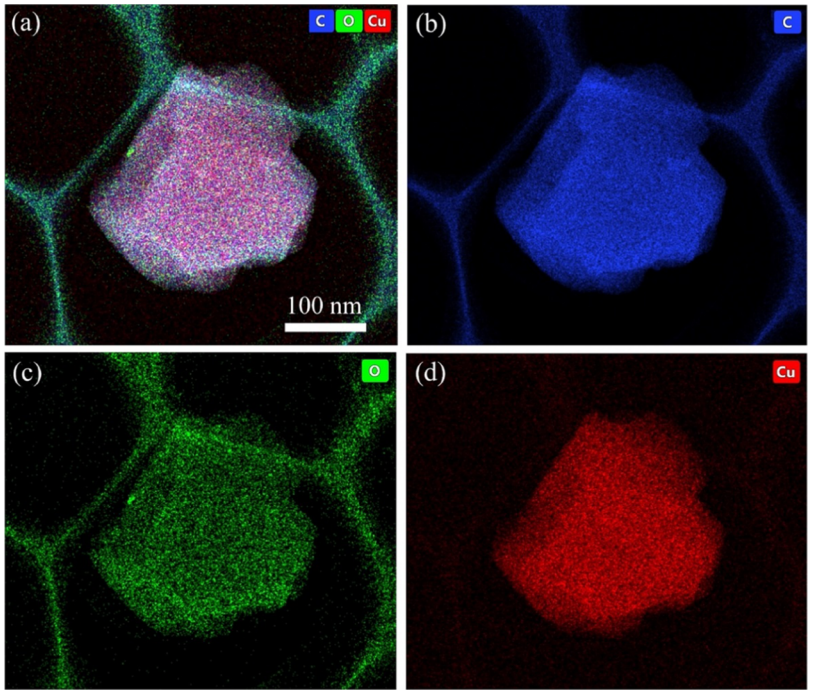

Figure 4. EDX mapping images of the as-prepared $Cu_xO@C_{18}H_{36}O_2$ nanocomposite: (a) denotes the presence of elements combined together, (b) carbon element, (c) oxygen, and (d) copper element.

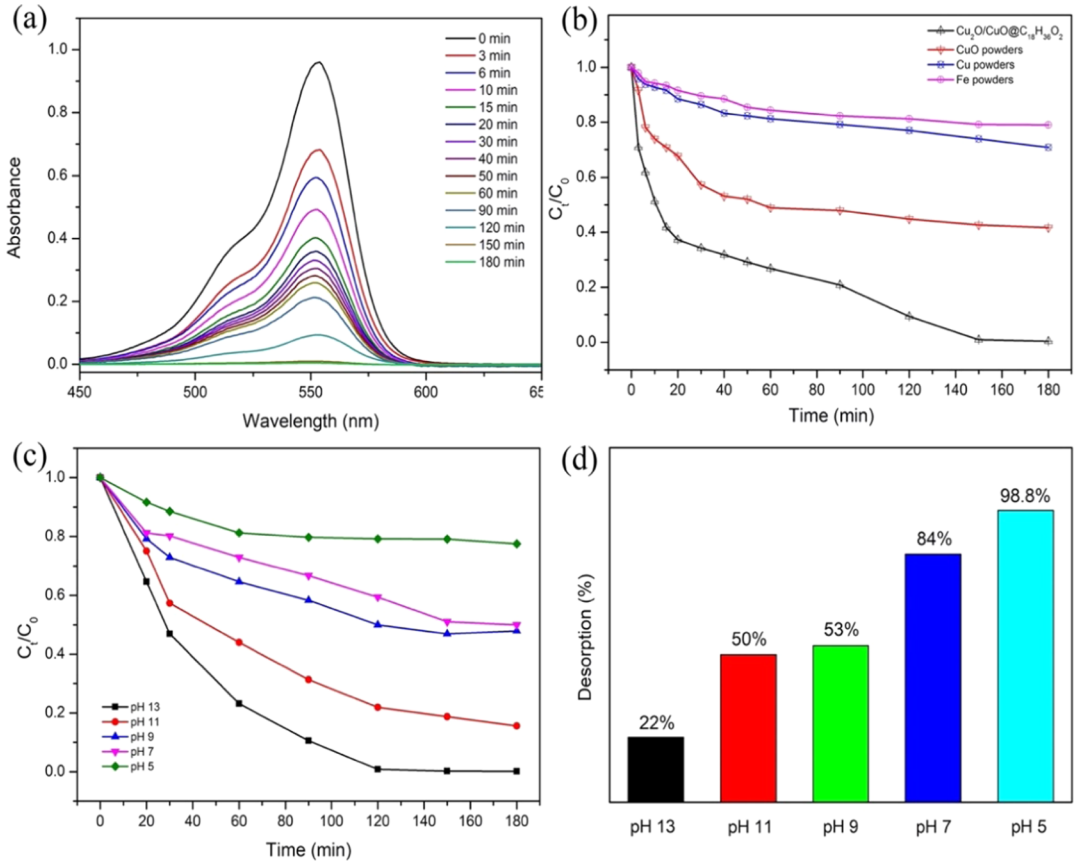

Figure 5. (a) UV absorption spectra for RhB in different reaction times (20 mg/L dye concentration, pH = 7). (b) RhB adsorption performance in different systems (pH = 7). (c) Effect of pH on the adsorption of the RhB dyes. (d) Desorption efficiency versus pH rates.

sample had a negative charge ζ potential (−38.75 to −60.30 mV). It is stated that even more cationic ions extracted from RhB would be driven into the stern layer (compact sheet) by increasing the concentration of H^+ ions, owing to electrostatic repulsion, thereby stimulating the movement of electrons from RhB to the $Cu_xO@C_{18}H_{36}O_2$ catalyst and enhancing the Fenton

https://doi.org/10.1021/acsomega.1c02881
ACS Omega 2021, 6, 22188−22201

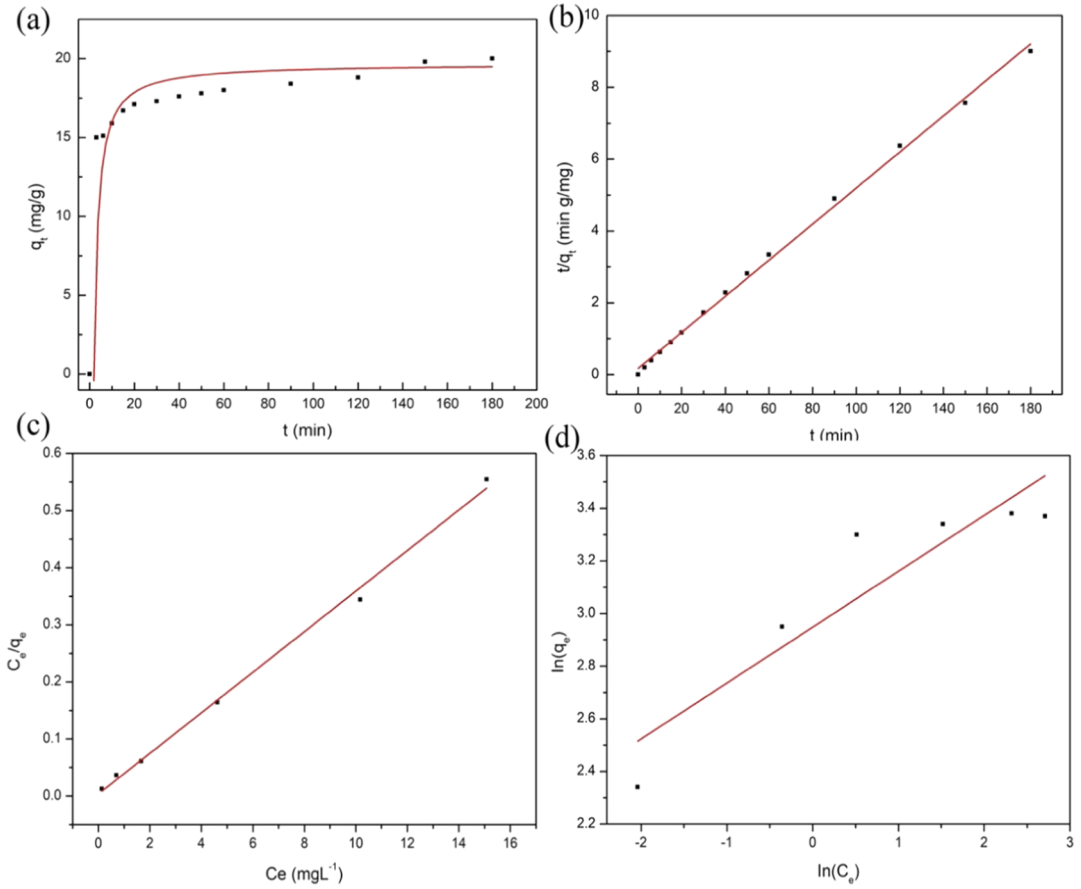

Figure 6. (a) Pseudo-first-order kinetic plot and (b) pseudo-second-order kinetic plot for the degradation of RhB in the presence of the Cu_xO@$C_{18}H_{36}O_2$ catalyst. (c) Langmuir isotherm model and (d) Freundlich isotherm model for RhB dyes.

catalytic performance of the catalyst. Moreover, increasing the concentration of OH^- ions and more cationic ions in the diffusion layer owing to the electrostatic attraction between the dye molecule and catalyst hinder their electron transfer. As a result, it can be concluded that a more alkaline environment would be benefited for efficient adsorption. As seen in Figure 4, the energy-dispersive X-ray (EDX) mapping profile reveals the existence of elements and uniform distribution of carbon, oxygen, and copper components in the produced nanocomposite powder. In addition, Cu_2O and CuO exist both for the transfer of charges and improving catalytic reactions.[52] The specific Cu_xO/stearic acid compound prevents the direct contact of activated Cu^+/Cu^{2+} with an acidic or alkaline solution, while it provides charge transfer for RhB dye degradations.[53]

Adsorption Studies of Dyes. Adsorption of RhB dyes from an aqueous solution is successfully responded through the synthesized Cu_xO@$C_{18}H_{36}O_2$ catalyst. The change in UV−vis absorption spectra for the initial concentration of 20 mg/L RhB dye solution (λ_{max} = 553 nm) was studied for the Cu_xO@$C_{18}H_{36}O_2$ catalyst without H_2O_2 at different reaction times (shown in Figure 5a). The adsorption efficiency of the catalyst for the removal of RhB dye was further examined. The dye removal efficiency (R%) was calculated using eq 3.

$$R\% = (C_0 - C_t) \times 100/C_0 \quad (3)$$

Here, the initial and final concentrations of dyes are denoted by C_0 (mg/L) and C_t (mg/L), respectively.

The adsorption capacity at equilibrium (q_e) was calculated using eq 4.

$$q_e = (C_0 - C_e)V/W \quad (4)$$

where C_0 and C_e (mg/L) are the initial and equilibrium concentrations of dye solutions, respectively. Also, the volume of dye solution V (L) and weight of the adsorbent W (mg/L) were added to the experimental solution.

As illustrated in Figure 5a, the Cu_xO@$C_{18}H_{36}O_2$ catalyst absorption efficiency was evaluated through UV−vis absorption spectra for the abovementioned dye solution at room temperature. At the initial reaction time of 3 min, a significant decrease in adsorption was observed, but with gradually increasing reaction time, the dye concentration declined steadily, becoming almost flat after 180 min (equilibrium point) at pH 13. Furthermore, Figure 5b compares CuO, Cu, and Fe powders as a function of the reaction time at room temperature in alkaline conditions (pH 13). The C_t/C_0 of RhB shows that CuO and Cu powders slightly decrease the dye concentration with the reaction time, and Fe powders degrade by a significant amount, while the Cu_xO@$C_{18}H_{36}O_2$ composite exhibits an excellent absorbance performance and shows much higher adsorption activity of 99% of RhB after 180 min.

The pH level in the reaction system is closely linked to the absorbance efficiency.[54] The adsorption behavior was studied in the pH range of 5−13. As shown in Figure 5c, the adsorbent surface was prone to have a net positive charge, and therefore, the cationic dye (RhB) adsorption is very low due to the repulsive forces between the positive surface of the adsorbent

https://doi.org/10.1021/acsomega.1c02881
ACS Omega 2021, 6, 22188−22201

and the cationic dye molecules when the pH is below 5.0. On the other hand, while the solution pH was above 7, the adsorbent surface was likely to have a net negative charge that enhanced the adsorption of cationic dye at about 50% of adsorption, and on gradually increasing the pH value, the amount of dye adsorption notably increased and reached almost 99% at the high alkaline condition (pH 13). The results suggest that the principal adsorption mechanism is attributed to the electrostatic interaction between the negative adsorbent surface and the positive part of the dye molecules. The desorption efficiency versus pH rate shown in Figure 5d indicates that at pH 13, the desorption of RhB was only 22% and gradually increased with the decrease of pH levels, with 98.8% desorption rate being achieved at pH 5, revealing that the pH value plays a key role in the desorption mechanism. The carboxyl groups on the dye molecule were disassociated in a lower pH solution, which deteriorated the interaction between the RhB and the catalyst. Therefore, the analysis mentioned above implies that this system could efficiently operate adsorption−desorption under near-neutral and alkalic conditions.

Adsorption Kinetics. A kinetic study was designed to evaluate the dye adsorption behavior. The kinetic mechanism, which determines the process of adsorption, was assessed by performing pseudo-first-order and pseudo-second-order model equations. The pseudo-first-order kinetic mechanism is prompted by eq 5

$$\log(q_e - q_t) = \log(q_e) - k_1 t/2.303 \quad (5)$$

where k_1 is the rate constant of the reaction, q_e and q_t indicate the amount of dye adsorbed at equilibrium and time t, respectively. The plot of log $(q_e - q_t)$ vs t describes the adsorption of dyes on the nanocomposite. The pseudo-second-order kinetic mechanism is expressed by eq 6

$$t/q_t = 1/k_2 q_e^{\ 2} + t/q_e \quad (6)$$

where k_2 is the second-order rate constant, q_t and q_e represent the amount of adsorbate adsorbed at equilibrium and time t, respectively. Here, the nonlinear plot q_t versus t (Figure 6a) and the linear plot of t/qt versus t (Figure 6b) are shown. The correlation (R^2) values are 0.85 and 0.99 (Table 1) for the pseudo-first-order and pseudo-second-order kinetics mechanisms, respectively. It reveals that the dye adsorption on the surface of the $Cu_xO@C_{18}H_{36}O_2$ nanocomposite agreed with the pseudo-second-order kinetics mechanism.

Table 1. Fitting Data of Adsorption Kinetics and Isotherms

(a) Adsorption kinetic models					
Pseudo-first-order model			Pseudo-second-order model		
k_1 (g/mg/min)	q_e (mg/g)	R^2	k_2 (g/mg/min)	q_e (mg/g)	R^2
0.163	16.67	0.846	0.01139	20.06	0.998
(b) Adsorption isotherms					
Langmuir isotherm			Freundlich isotherm		
q_{max} (mg/g)	K_L (L/g)	R_L R^2	K_f ($mg^{1-1/n}.L^{1/n}.g^{-1}$)	n	R^2
28.24	1.167	0−1 0.997	316.22	0.213	0.849

Adsorption Isotherms. Two forms of isotherm models, the Langmuir and Freundlich models, have been used to evaluate the adsorption potential and mechanism of adsorption. Langmuir isotherm is based on the premise that monolayer adsorption happens with a small number of equivalent adsorption sites on the adsorbent surface, represented by eq 7.

$$C_e/q_e = C_e/q_{max} + 1/(q_{max}K_L) \quad (7)$$

Here, C_e denotes the equilibrium concentration, q_e and q_{max} denote the equilibrium and optimum adsorption capacities, and K_L denotes the Langmuir constant. Using eq 7, a C_e/q_e vs C_e graph was plotted and found to be linear, as seen in Figure 6c. The values of K_L and q_{max} determined by the slope and intercept of the linear curve achieved from the Langmuir isotherm equation are listed in Table 1. Freundlich isotherm is based on the premise that the adsorbent surface is exposed to heterogeneous adsorption. It is represented by eq 8.

$$\ln q_e = 1/n\ (\ln\ C_e) + \ln K_f \quad (8)$$

Here, q_e and C_e denote the quantity of adsorption and concentration of the equilibrium solutions, n denotes the extent of heterogeneity of the surface, and K_f is the Freundlich constant indicating the adsorption potential.

The Freundlich isotherm (Figure 6d) was used to quantify the values of n, K_f, and q_e summarized in Table 1. The correlation coefficient value (R^2) derived in the case of Langmuir isotherm (0.99) was found to be higher in comparison to Freundlich isotherm (0.85) (Table 1). This revealed that the Langmuir isotherm model performed better than the Freundlich adsorption model, and monolayer adsorption of dye occurs on the surface of $Cu_xO@C_{18}H_{36}O_2$. The $1/n$ value of RhB (in the limit of 0.6−1) and the large value of q_{max} measured from Langmuir isotherm indicate the higher adsorption capacity of the catalyst.

A number of classical adsorption dynamic models could be used to evaluate mass transfer and the critical stages that controlled the reaction rate during adsorption. The Weber−Morris intraparticle diffusion model is utilized in this study; the formula is presented in eq 9

$$qt = K_{ip}(t)^{1/2} + C \quad (9)$$

Here, K_{ip} is the diffusion rate constant ($mg{\cdot}g^{-1}{\cdot}min^{-1}$) used to indicate the amount of absorption per unit of time, qt is the absorption capacity by unit mass catalysts at t ($mg{\cdot}g^{-1}$), and C is a constant and linked to the thickness of the boundary layer.

It is illustrated in Figure S3 that the adsorption process underwent three stages. In phase I, the precipitous line showed the rapidly increasing absorption of the $Cu_xO@C_{18}H_{36}O_2$ nanocomposite. The RhB molecules in the solution spread to the liquid membrane attached to the $Cu_xO@C_{18}H_{36}O_2$ nanocomposite catalyst surface and then broke through. Followed by catalyst surface diffusion, they gradually reached the active site. At this stage, electrostatic adsorption was the main driving force. In stage 2, the dye molecules dispersed through the pores of the nanoporous copper framework. When the dye molecules reached the inner pore passages, they formed a competitive interaction with one another, leading to diffusion resistance. As a result, the diffusion rate constant was noticeably less than that in the first stage. The slope value of the third stage was significantly zero in stage 3. The adsorption active sites on the surface of the catalyst had been utilized to near saturation after the rapid molecular movement and diffusion via the pore interface of the first two phases. A dynamic equilibrium process between adsorption and desorption was exhibited at this point, and the diffusion rate constant was near zero.

https://doi.org/10.1021/acsomega.1c02881
ACS Omega 2021, 6, 22188−22201

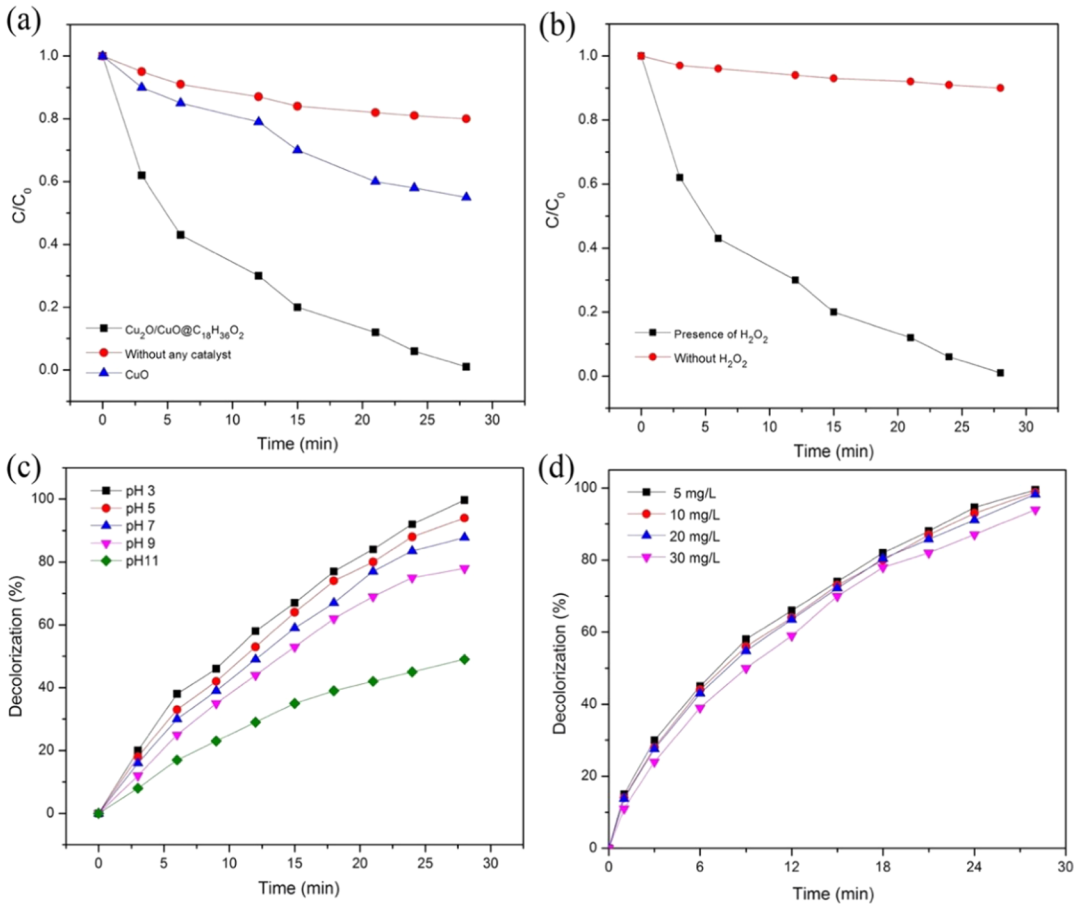

Figure 7. (a) Degradation performance of RhB over $Cu_xO@C_{18}H_{36}O_2$ and comparison with different catalysts (pH = 3.0, H_2O_2 = 0.05 M, 20 mg L^{-1}). (b) $Cu_xO@C_{18}H_{36}O_2$ catalytic effect on the degradation of RhB in the presence and absence of H_2O_2 (pH = 3.0, 20 mg L^{-1}). (c) Effect of initial pH on the decolorization of RhB (H_2O_2 = 0.05 M, 20 mg L^{-1}). (d) Effect of initial dye concentration on the Fenton-like degradation of RhB (temperature: 25 °C, pH 3, H_2O_2 = 0.05 M).

A nonlinear curve fitted with the Langmuir model on BET adsorption data has a good correlation with an R^2 value of 0.61 (p-value < 0.001). This nonlinearized isotherm expression showed (in Figure S5) significant similarity with our experimental results.

Catalytic Degradation of RhB. As a demonstration of the application of $Cu_xO@C_{18}H_{36}O_2$, the organic cationic dyestuff RhB was selected to assess the catalytic performance. Figure 7 demonstrates the catalytic performance at different conditions for the degradation of RhB in the presence of H_2O_2. As shown in Figure 7a, in the absence of catalysts, RhB was degraded slightly by H_2O_2. Besides, degradation of RhB was moderately enhanced by the catalyst's CuO or Cu_2O nanoparticles and in the presence of H_2O_2. The catalytic oxidation of RhB happened via CuO/Cu_2O, and the adsorption was increased because of its negative surface, which suggests the excellent catalytic ability of synthesized catalysts. However, no obvious catalytic activity was observed in the absence of H_2O_2 (Figure 7b). It can be noticed that the strong catalytic efficiency of $Cu_xO@C_{18}H_{36}O_2$ appeared mainly due to the rapid adsorption of RhB molecules to the catalyst by $\pi-\pi$ stacking interactions between RhB and the π-conjugation mechanism of the catalyst, as well as the two-dimensional planar structure contributing to the fast degradation of RhB.[55]

Effect of Initial pH. In Fenton's reaction, one of the key parameters is pH value, and it has been stated that the optimum pH value is about 2−4 for the traditional Fenton reactions.[56,57] Tests were carried out to degrade RhB at different initial pH values. Figure 7c shows that the RhB decolorization rates for pH values of 3, 5, 7, 9, and 11 achieved 99.2, 94.1, 88.5, 78.1, and 49.5%, respectively. The findings showed a remarkable degradation efficiency against RhB within a broad operating pH range of 3−11, suggesting that stearic acid coupled with copper oxide could transcend the limitation of a rigorous pH scale of the homogeneous Fenton method. It is reported that the decolorization value improved as the pH level reduced, approaching a maximum at pH 3.[58] RhB is a cationic dye and its degradation rate is maximum at a low pH range. A higher decolorization rate for copper at a lower pH is due to a stronger ability to extract Cu^{2+} ions from the oxide substrate.[59] Meanwhile, in this section, stearic acid could act as a H^+ donor, provide relatively stable pH environment, expand the range of the initial equilibrium pH to the neutral condition, and perform about 88% degradation of dyes. However, as the pH of the solution approached 11, precipitation occurred, suggesting that the reaction was almost entirely suppressed.

Effect of Initial Dye Concentration. Figure 7d represents the decolorization of RhB at several initial dye concentrations, fixing the amount of the H_2O_2 concentration (0.05 M) and the pH value (3.0). It can be noticed that a higher dye concentration led to a considerable decrease in the decolorization rate. This may be attributed to the lack of accumulation of hydroxyl radicals that react with a higher volume of dye in the solution. Even decolorization of RhB reduced at the initial concentration

https://doi.org/10.1021/acsomega.1c02881
ACS Omega 2021, 6, 22188−22201

of 5−30 mg L^{-1}, implying the significant potential of the Fenton system treating the high concentration of organic compounds. However, beyond a certain level, the dye molecules would be inadequate for adsorption with a large number of active sites, resulting in no significant changes in the degradation process. A concentration of 20 mg L^{-1} of RhB was chosen for adsorption and catalytic degradation of dye.

Recyclability of the Catalyst. The reusability and durability of the as-prepared catalyst were evaluated by reusing the catalyst in a fresh mixture of RhB and H_2O_2 solution. Figure 8 depicts the RhB decolorization recycling experiments for six

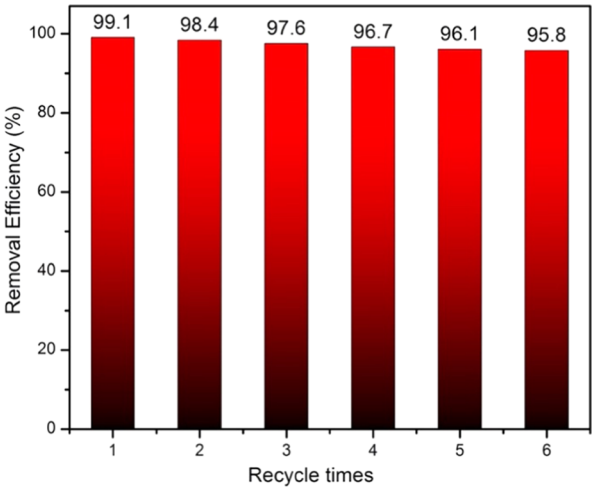

Figure 8. Recycling experiments of RhB decolorization for six cycles (pH = 3.0, H_2O_2 = 0.05 M, dye concentration = 20 mg L^{-1}, 10 mg of catalyst).

cycles. It shows that the initial cycle degraded 99.1% of RhB and about 95.8% of RhB degraded after the six repetitive cycles. The catalytic activity of the catalyst exhibited a minor difference, implying the high stability during the Fenton catalytic reaction. Also, Figure S1 shows a FESEM image of the catalyst with a slight change in morphology after six cycles of catalytic degradation, but no noticeable changes were found after the reaction in elemental groups (shown in Figure S4). The significant improvement in the catalytic operation of the catalyst was due to its optical efficiency and specific structural properties. The porous hierarchical $Cu_xO@C_{18}H_{36}O_2$ structures have a high active surface area and significant pore size of the nanoflakes that offer additional space and suitable pathways for fast and rapid diffusion of the organic dye molecules through the internal surface during the heterogeneous catalytic reaction.[60]

Adsorption and Degradation Mechanism. A potential mechanistic pathway for the Fenton oxidative degradation of organic pollutants over the $Cu_xO@C_{18}H_{36}O_2$ catalyst was presented based on the nanostructure characterization and RhB degradation experiments stated above. The degradation mechanism can usually be divided into two subprocesses: adsorption process and catalytic reaction.[61] In terms of adsorption, $Cu_xO@C_{18}H_{36}O_2$ has a large specific surface area (51.4 m^2 g^{-1}), which plays a dominant role as it offers a wide region of adsorption area and the copious unique structure of atomic steps existing on the surface of the catalyst (Scheme 2) can provide distinctive surface-active sites for the strong adsorption of dye molecules.[62] Besides, this might improve the interaction between the catalyst and organic contaminants and make it more favorable for degradation reactions.[63,64] It is also proposed that the existence of oxygen vacancies in the system can provide a negative charge surface that could improve the electrostatic contact between the catalyst surface and the cationic dye molecules.[65] As far as the catalytic reaction is concerned, it is well known that the typical Fenton reaction is characterized by the response of aqueous Fe^{2+} with H_2O_2 to produce a $HO^{\bullet}$ radical, which is the dominant oxidizing agent and interacts with dyes to decolorate them. The volume of the $HO^{\bullet}$ radical generated in the Fenton system increased gradually with increasing reaction time.[66] The advanced Fenton method is stated to apply the solid surface of zero-valent iron (ZVI) to produce Fe^{2+}, thus leading to a Fenton-like reaction.[67] Likewise, Cu^0 also generates Cu^+ and catalyzes the decomposition of H_2O_2 to create $HO^{\bullet}$ radicals.[68,69] Given below is the well-established Fenton-like reaction of Cu^0.

$$\text{Surface} - Cu^0 + H_2O_2 \rightarrow Cu^{2+} + 2OH^- \quad (10)$$

$$Cu^{2+} + H_2O_2 \rightarrow Cu^+ + H^+ + HO^{\bullet} \quad (11)$$

$$Cu^+ + H_2O_2 \rightarrow Cu^{2+} + OH^- + HO^{\bullet} \quad (12)$$

It is shown that the activation of H_2O_2 by the Cu^0 catalyst can be achieved via a sequence of electron transfer processes between Cu^{2+}, Cu^+, and Cu^0 ions. The high degradation of the Fenton-like oxidation with Cu^0 is a source to produce cupric ions via eqs 10−12 in neutral pH. The reaction mechanism also proposed the dye degradation initiation with the adsorption of H_2O_2 on the surface, while subsequent reactions occurred between H_2O_2 and Cu_2O under the acidic conditions (pH < 4) and generated $HO^{\bullet}$ radicals and then attacked dye molecules as well as organic intermediates to degrade completely, as described in reactions (eqs 13 and 14) below.[52]

$$\text{Surface} - Cu^+ + H_2O_2 \rightarrow Cu^{3+}(aq) \quad (13)$$

$$Cu^{3+}(aq) \rightarrow H_3O^+ + Cu^{2+}(aq) + HO^{\bullet} \quad (14)$$

CONCLUSIONS

In this work, we have successfully synthesized a low-cost, high-performance nanoflakes $Cu_xO@C_{18}H_{36}O_2$ catalyst through a facile hydrothermal method, with the stearic acid being shielded by copper oxide nanoparticles. Owing to the unique nanoflake morphology and a high specific surface area of ∼51.4 m^2 g^{-1}, the as-prepared catalyst shows a high degradation efficiency of about ∼99% for RhB. The degradation process is more efficient because of the synergistic effects of adsorption and degradation that happened simultaneously. The high degradability of the RhB dye is attributed to the generation of HO radicals via Cu_2O/H_2O_2 reactions under acidic conditions and CuO/H_2O_2 reactions in neutral pH. Furthermore, due to the long-chain hydrophobic tail of copper stearate, hydrophobic functional groups could interact with dyes. The adsorption could be performed under near-neutral and alkali conditions, and also the prepared catalyst showed good reusability performance in a neutral condition. The present work indicates that $Cu_2O/CuO@C_{18}H_{36}O_2$-$H_2O_2$ could be a high-efficiency Fenton-like reagent for achieving complete degradation of cationic azo dyes and drives a potential application in wastewater treatments.

https://doi.org/10.1021/acsomega.1c02881
ACS Omega 2021, 6, 22188−22201

Scheme 1. Synthesis Process of the As-Prepared $Cu_xO@C_{18}H_{36}O_2$ Nanocomposite Catalyst

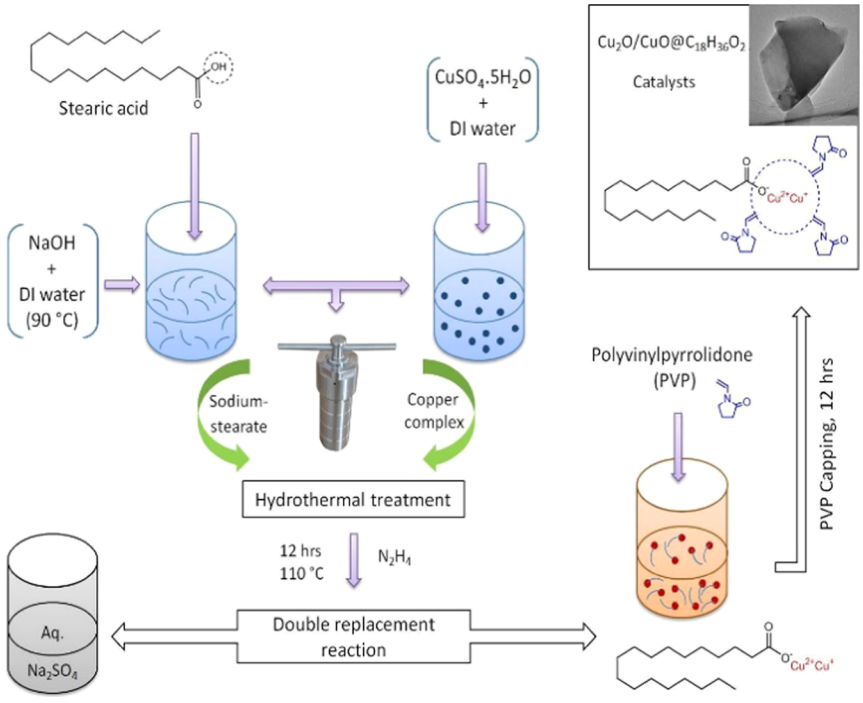

Scheme 2. Proposed Mechanism for the Enhanced Adsorption and Degradation Reaction of RhB

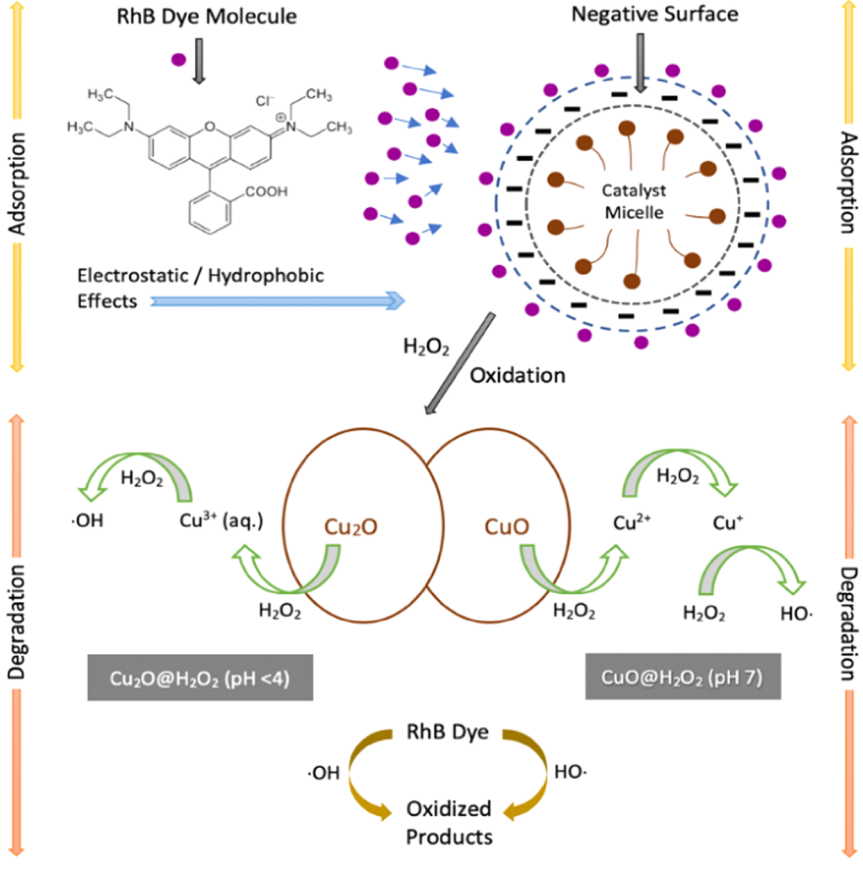

EXPERIMENTAL SECTION

Materials and Reagents. Stearic acid ($C_{18}H_{36}O_2$), copper sulfate pentahydrate ($CuSO_4{\cdot}5H_2O$), hydrogen peroxide (H_2O_2, 30 wt %), sodium hydroxide (NaOH), and ethanol (C_2H_5OH) were purchased from Aladdin Reagent Co., China. Poly(vinylpyrrolidone) (PVP) (M_w = 40 000) and hydrazine hydrate (N_2H_4 50−60%) were obtained from Sigma-Aldrich, China. Rhodamine B (RhB) was purchased from Sinopharm

https://doi.org/10.1021/acsomega.1c02881
ACS Omega 2021, 6, 22188−22201

Chemical Reagent Co., Ltd., Shanghai, China. The chemicals were used without further purification, and purified deionized water was used to prepare aqueous solutions.

Preparation of Sodium Stearate Powder. At first, 1 gm of stearic acid was melted at 90 °C temperature for 30 min and then 20 mL of hot water was added and continued to stir in a water bath condition for 30 min to form a uniform solution (solution A). After that, an aqueous solution of 2 gm of NaOH pre-dissolved in 20 mL of water and the aqueous solution was mixed with solution A and stirred for 6 h while maintaining a constant temperature of 90 °C. This reaction neutralized the stearic acid and produced water-soluble sodium salt of stearic acid. The synthesized materials were washed with 50 mL of ethanol and dried at room temperature for 2 h. Sodium stearate powder was obtained with a yield of ∼2.5 g.

Synthesis of $Cu_xO@C_{18}H_{36}O_2$. To perform a double replacement reaction for the preparation of the catalysts; 2 g of sodium stearate was taken in a beaker and dissolved into 40 mL of water (solution B). In a separate beaker, 2 g of $CuSO_4 \cdot 5H_2O$ was dissolved into 50 mL of water and mixed with solution B with continuous stirring for 1 h at room temperature. Then, 0.5−1 mL of hydrazine hydrate was added dropwise into the solution and stirred for 30 min at room temperature (solution C). After that, solution C was transferred into a Teflon-lined autoclave for hydrothermal treatment for 12 h in an oven at 110 °C to obtain the precipitated $Cu_xO@C_{18}H_{36}O_2$ nanocomposite. The precipitation confirmed that the double replacement reaction took place between sodium stearate and corresponding copper complexes of aqueous $CuSO_4 \cdot 5H_2O$. Then, the prepared nanocomposites were mixed with a predissolved 100 mL of PVP (1.5 gm) aqueous solution and continued to stir at room temperature for 4 h and aged for 12 h to complete the capping of the prepared $Cu_xO@C_{18}H_{36}O_2$ nanocomposite. The excess PVP was removed by centrifuging at 6000 rpm for 8 min using ethanol and pure water three times. Finally, the synthesized PVP-capped $Cu_xO@C_{18}H_{36}O_2$ nanocomposite was dried at room temperature for 24 h and the final samples were collected for further usage. Scheme 1 shows the synthesis steps of as-prepared nanocomposite catalysts.

Materials Characterization. The morphology and particle size of materials were recorded using a JSM 7600F field-emission scanning electron microscope (FESEM) (JEOL, Japan). Transmission electron microscopy (TEM) and energy-dispersive X-ray (EDX) mapping were conducted with a FEI Titan G2 60−300 instrument. Fourier transform infrared (FT-IR) spectroscopy (VERTEX-70) was used to obtain the functional groups of the sample. The X-ray diffraction (XRD) patterns of the catalysts were measured using Panalytical X'pert PRO MRD (Holland) with Cu Kα radiation. The X-ray photoelectron spectroscopy (XPS) by an AXIS-ULTRA DLD 600W was used to study the structural properties of the catalysts. The specific surface area, total pore volume, and average pore diameter of the nanocomposite catalysts were measured by the conventional Brunauer−Emmett−Teller (BET, TriStar II 3020) technique. The colloidal electrokinetic potential analysis was performed using a zeta analyzer (Malvern Zeta Analyzer, ZEN3690) to determine the nature of surface charges of the catalyst in different pH values. The UV absorption spectra of the dye concentration were received by a PerkinElmer Lambda 35 UV−vis spectrophotometer (Scheme 2).

Adsorption Experiments. The dye adsorption experiments of the synthesized catalyst were performed without H_2O_2, where 10 mg of $Cu_xO@C_{18}H_{36}O_2$ adsorbent was added into 60 mL of RhB dye/water solution (20 mg/L, pH = 7) under continuous stirring at ambient temperature. To prevent the influence of light, the whole process had been carried out in a black box without any light sources. To monitor the adsorption process, the dye solution samples for analysis were taken out from the reactor at different time intervals and filtered with a cellulose acetate syringe. Afterward, the UV−vis absorption spectra of the filtered dye solution were recorded. At the end of the adsorption process, the residue adsorbents were collected from the solution through centrifugation and cleaned by deionized water and then with ethanol three times before the following desorption−adsorption cycle.

Degradation Experiments. The catalytic behavior of the prepared $Cu_xO@C_{18}H_{36}O_2$ nanocomposite was evaluated for the degradation of a model azo dye rhodamine B (RhB). Experiments were conducted in a 100 mL glass Erlenmeyer flask, equipped with a water bath heating system and constant stirrings. To avoid light interference, the entire activity was conducted in a black box with no light sources. At the first stage, pH values of RhB dye solutions were calibrated either by 1 M HCl or 1 M NaOH solution. Then, 10 mg of $Cu_xO@C_{18}H_{36}O_2$ nanocomposite was added into 60 mL of RhB aqueous solution (pH = 3.0, H_2O_2 = 0.05 M, 20 mg L^{-1}) and the catalytic degradation of dyes was executed.

■ ASSOCIATED CONTENT

Supporting Information

The Supporting Information is available free of charge at https://pubs.acs.org/doi/10.1021/acsomega.1c02881.

FESEM image of the catalyst after six repetition cycles of the catalytic reaction (Figure S1); TEM and HRTEM (insert) image of the as-prepared catalyst (Figure S2); the intraparticle diffusion model for the $Cu_xO@C_{18}H_{36}O_2$ nanocomposite catalyst (Figure S3); XRD patterns before and after the cycling catalytic experiments (Figure S4); and BET adsorption isotherm investigated by nonlinear models (Figure S5) (PDF)

■ AUTHOR INFORMATION

Corresponding Author

Yue Xu − *School of Materials Science and Engineering and State Key Laboratory for Materials Processing and Die & Mould Technology, Huazhong University of Science and Technology, Wuhan 430074, People's Republic of China*; Email: xuyue@hust.edu.cn

Authors

Ratul Rehman − *School of Materials Science and Engineering and State Key Laboratory for Materials Processing and Die & Mould Technology, Huazhong University of Science and Technology, Wuhan 430074, People's Republic of China*

Sudip Kumar Lahiri − *School of Materials Science and Engineering and State Key Laboratory for Materials Processing and Die & Mould Technology, Huazhong University of Science and Technology, Wuhan 430074, People's Republic of China*; orcid.org/0000-0002-4559-4880

Ashraful Islam − *State Key Laboratory of Environmental Aquatic Chemistry, Research Center for Eco-Environmental Sciences, University of Chinese Academy of Sciences, Chinese Academy of Sciences, Beijing 100085, China*

Peng Wei − *School of Materials Science and Engineering and State Key Laboratory for Materials Processing and Die &*

Mould Technology, Huazhong University of Science and Technology, Wuhan 430074, People's Republic of China

Complete contact information is available at:
https://pubs.acs.org/10.1021/acsomega.1c02881

Notes

The authors declare no competing financial interest.

■ ACKNOWLEDGMENTS

This research was supported by the National Natural Science Foundation of China (Grants 51772117, 51902118, and 51732005). The key Research and Development Programs of Hubei Province, China (No. 2019AAA019). The authors also praise HUST's Analytical and Testing Centre and the State Key Laboratory of Materials Processing and Die & Mold Technology of HUST for FT-IR, XRD, SEM, TEM, and other tests.

■ REFERENCES

(1) Pinto, M. B.; Samanamud, G. R. L.; Baston, E. P.; França, A. B.; Naves, L. L. R.; Loures, C. C. A.; Naves, F. L. Multivariate and Multiobjective Optimization of Tannery Industry Effluent Treatment Using Musa Sp Flower Extract in the Coagulation and Flocculation Process. *J. Cleaner Prod.* **2019**, *219*, 655−666.

(2) Natarajan, S.; Bajaj, H. C.; Tayade, R. J. Recent Advances Based on the Synergetic Effect of Adsorption for Removal of Dyes from Waste Water Using Photocatalytic Process. *J. Environ. Sci.* **2018**, *65*, 201−222.

(3) Zhao, T.; Li, P.; Tai, C.; She, J.; Yin, Y.; Qi, Y.; Zhang, G. Efficient Decolorization of Typical Azo Dyes Using Low-Frequency Ultrasound in Presence of Carbonate and Hydrogen Peroxide. *J. Hazard. Mater.* **2018**, *346*, 42−51.

(4) Punzi, M.; Anbalagan, A.; Aragão Börner, R.; Svensson, B. M.; Jonstrup, M.; Mattiasson, B. Degradation of a Textile Azo Dye Using Biological Treatment Followed by Photo-Fenton Oxidation: Evaluation of Toxicity and Microbial Community Structure. *Chem. Eng. J.* **2015**, *270*, 290−299.

(5) Bao, S.; Yang, W.; Wang, Y.; Yu, Y.; Sun, Y. Highly Efficient and Ultrafast Removal of Cr(VI) in Aqueous Solution to Ppb Level by Poly(Allylamine Hydrochloride) Covalently Cross-Linked Amino-Modified Graphene Oxide. *J. Hazard. Mater.* **2021**, *409*, No. 124470.

(6) Meng, X.; Liu, Y.; Han, G.; Yang, W.; Yu, Y. Three-Dimensional (Fe3O4/ZnO)@C Double-Core@shell Porous Nanocomposites with Enhanced Broadband Microwave Absorption. *Carbon* **2020**, *162*, 356−364.

(7) Malato, S.; Fernández-Ibáñez, P.; Maldonado, M. I.; Blanco, J.; Gernjak, W. Decontamination and Disinfection of Water by Solar Photocatalysis: Recent Overview and Trends. *Catal. Today* **2009**, *147*, 1−59.

(8) Bláha, M.; Riesová, M.; Zedník, J.; Anžlovar, A.; Žigon, M.; Vohlídal, J. Polyaniline Synthesis with Iron(III) Chloride-Hydrogen Peroxide Catalyst System: Reaction Course and Polymer Structure Study. *Synth. Met.* **2011**, *161*, 1217−1225.

(9) Wang, N.; Zheng, T.; Zhang, G.; Wang, P. A Review on Fenton-like Processes for Organic Wastewater Treatment. *J. Environ. Chem. Eng.* **2016**, *4*, 762−787.

(10) Aramyan, S. M. Advances in Fenton and Fenton Based Oxidation Processes for Industrial Effluent Contaminants Control-A Review. *Int. J. Environ. Sci. Nat. Resour.* **2017**, *2*, 115−132.

(11) Liu, X.; Liu, H.; Wang, Y.; Yang, W.; Yu, Y. Nitrogen-Rich g-C3N4@AgPd Mott-Schottky Heterojunction Boosts Photocatalytic Hydrogen Production from Water and Tandem Reduction of NO3− and NO2−. *J. Colloid Interface Sci.* **2021**, *581*, 619−626.

(12) Lee, H.; Lee, H. J.; Seo, J.; Kim, H. E.; Shin, Y. K.; Kim, J. H.; Lee, C. Activation of Oxygen and Hydrogen Peroxide by Copper(II) Coupled with Hydroxylamine for Oxidation of Organic Contaminants. *Environ. Sci. Technol.* **2016**, *50*, 8231−8238.

(13) Jin, H.; Tian, X.; Nie, Y.; Zhou, Z.; Yang, C.; Li, Y.; Lu, L. Oxygen Vacancy Promoted Heterogeneous Fenton-like Degradation of Ofloxacin at PH 3.2-9.0 by Cu Substituted Magnetic Fe3O4@FeOOH Nanocomposite. *Environ. Sci. Technol.* **2017**, *51*, 12699−12706.

(14) Ling, Y.; Long, M.; Hu, P.; Chen, Y.; Huang, J. Magnetically Separable Core-Shell Structural γ-Fe2O3@Cu/Al-MCM-41 Nanocomposite and Its Performance in Heterogeneous Fenton Catalysis. *J. Hazard. Mater.* **2014**, *264*, 195−202.

(15) Soler, J.; García-Ripoll, A.; Hayek, N.; Miró, P.; Vicente, R.; Arques, A.; Amat, A. M. Effect of Inorganic Ions on the Solar Detoxification of Water Polluted with Pesticides. *Water Res.'* **2009**, *43*, 4441−4450.

(16) Luo, X.; Hu, H.; Pan, Z.; Pei, F.; Qian, H.; Miao, K.; Guo, S.; Wang, W.; Feng, G. Efficient and Stable Catalysis of Hollow Cu9S5 Nanospheres in the Fenton-like Degradation of Organic Dyes. *J. Hazard. Mater.* **2020**, *396*, No. 122735.

(17) Ye, Q.; Xu, H.; Wang, Q.; Huo, X.; Wang, Y.; Huang, X.; Zhou, G.; Lu, J.; Zhang, J. New Insights into the Mechanisms of Tartaric Acid Enhancing Homogeneous and Heterogeneous Copper-Catalyzed Fenton-like Systems. *J. Hazard. Mater.* **2021**, *407*, No. 124351.

(18) Mikami, K.; Kido, Y.; Akaishi, Y.; Quitain, A.; Kida, T. Synthesis of Cu 2 O/CuO Nanocrystals and Their Application to H 2 S Sensing. *Sensors* **2019**, *19*, 211.

(19) Luan, V. H.; Han, J. H.; Kang, H. W.; Lee, W. Highly Porous and Capacitive Copper Oxide Nanowire/Graphene Hybrid Carbon Nanostructure for High-Performance Supercapacitor Electrodes. *Composites, Part B* **2019**, *178*, No. 107464.

(20) Tamayo, L.; Azócar, M.; Kogan, M.; Riveros, A.; Páez, M. Copper-Polymer Nanocomposites: An Excellent and Cost-Effective Biocide for Use on Antibacterial Surfaces. *Mater. Sci. Eng., C* **2016**, *69*, 1391−1409.

(21) Shi, S.-C.; Peng, Y.-Q. Preparation and Tribological Studies of Stearic Acid-Modified Biopolymer Coating. *Prog. Org. Coatings* **2020**, *138*, No. 105304.

(22) Chang, Y.; Lye, M. L.; Zeng, H. C. Large-Scale Synthesis of High-Quality Ultralong Copper Nanowires. *Langmuir* **2005**, *21*, 3746−3748.

(23) Huang, H. H.; Yan, F. Q.; Kek, Y. M.; Chew, C. H.; Xu, G. Q.; Ji, W.; Oh, P. S.; Tang, S. H. Synthesis, Characterization, and Nonlinear Optical Properties of Copper Nanoparticles. *Langmuir* **1997**, *13*, 172−175.

(24) Barbosa, S.; Agrawal, A.; Rodríguez-Lorenzo, L.; Pastoriza-Santos, I.; Alvarez-Puebla, R. A.; Kornowski, A.; Weller, H.; Liz-Marzán, L. M. Tuning Size and Sensing Properties in Colloidal Gold Nanostars. *Langmuir* **2010**, *26*, 14943−14950.

(25) Bhajantri, R. F.; Ravindrachary, V.; Poojary, B.; Ismayil; Harisha, A.; Crasta, V. Studies on Fluorescent PVA + PVP + MPDMAPP Composite Films. *Polym. Eng. Sci.* **2009**, *49*, 903−909.

(26) Basha, M. A.-F. Magnetic and Optical Studies on Polyvinylpyrrolidone Thin Films Doped with Rare Earth Metal Salts. *Polym. J.* **2010**, *42*, 728−734.

(27) Su, Y.; Li, H.; Ma, H.; Wang, H.; Robertson, J.; Nathan, A. Dye-Assisted Transformation of Cu2O Nanocrystals to Amorphous CuxO Nanoflakes for Enhanced Photocatalytic Performance. *ACS Omega* **2018**, *3*, 1939−1945.

(28) Barati Darband, G.; Aliofkhazraei, M.; Khorsand, S.; Sokhanvar, S.; Kaboli, A. Science and Engineering of Superhydrophobic Surfaces: Review of Corrosion Resistance, Chemical and Mechanical Stability. *Arabian J. Chem.* **2020**, *13*, 1763−1802.

(29) Bensalem, S.; Hamdi, B.; Del Confetto, S.; Iguer-Ouada, M.; Chamayou, A.; Balard, H.; Calvet, R. Characterization of Chitosan/Montmorillonite Bionanocomposites by Inverse Gas Chromatography. *Colloids Surf., A* **2017**, *516*, 336−344.

(30) Liu, X.; Chen, J.; Liu, P.; Zhang, H.; Li, G.; An, T.; Zhao, H. Controlled Growth of CuO/Cu2O Hollow Microsphere Composites as Efficient Visible-Light-Active Photocatalysts. *Appl. Catal., A* **2016**, *521*, 34−41.

(31) Cioffi, N.; Ditaranto, N.; Torsi, L.; Picca, R. A.; Sabbatini, L.; Valentini, A.; Novello, L.; Tantillo, G.; Bleve-Zacheo, T.; Zambonin, P. G. Analytical Characterization of Bioactive Fluoropolymer Ultra-Thin

Coatings Modified by Copper Nanoparticles. *Anal. Bioanal. Chem.* **2005**, *381*, 607−616.
(32) Li, B.; Luo, X.; Zhu, Y.; Wang, X. Immobilization of Cu(II) in KIT-6 Supported Co 3 O 4 and Catalytic Performance for Epoxidation of Styrene. *Appl. Surf. Sci.* **2015**, *359*, 609−620.
(33) Biesinger, M. C.; Payne, B. P.; Grosvenor, A. P.; Lau, L. W. M.; Gerson, A. R.; Smart, R. S. C. Resolving Surface Chemical States in XPS Analysis of First Row Transition Metals, Oxides and Hydroxides: Cr, Mn, Fe, Co and Ni. *Appl. Surf. Sci.* **2011**, *257*, 2717−2730.
(34) Vieira, R. S.; Oliveira, M. L. M.; Guibal, E.; Rodríguez-Castellón, E.; Beppu, M. M. Copper, Mercury and Chromium Adsorption on Natural and Crosslinked Chitosan Films: An XPS Investigation of Mechanism. *Colloids Surf., A* **2011**, *374*, 108−114.
(35) Xu, J. F.; Ji, W.; Shen, Z. X.; Tang, S. H.; Ye, X. R.; Jia, D. Z.; Xin, X. Q. Preparation and Characterization of CuO Nanocrystals. *J. Solid State Chem.* **1999**, *147*, 516−519.
(36) Djellabi, R.; Ali, J.; Zhao, X.; Saber, A. N.; Yang, B. CuO NPs Incorporated into Electron-Rich TCTA@PVP Photoactive Polymer for the Photocatalytic Oxidation of Dyes and Bacteria Inactivation. *J. Water Process Eng.* **2020**, *36*, No. 101238.
(37) Djellabi, R.; Zhao, X.; Bianchi, C. L.; Su, P.; Ali, J.; Yang, B. Visible Light Responsive Photoactive Polymer Supported on Carbonaceous Biomass for Photocatalytic Water Remediation. *J. Cleaner Prod.* **2020**, *269*, No. 122286.
(38) Song, Y.-J.; Wang, M.; Zhang, X.-Y.; Wu, J.-Y.; Zhang, T. Investigation on the Role of the Molecular Weight of Polyvinyl Pyrrolidone in the Shape Control of Highyield Silver Nanospheres and Nanowires. *Nanoscale Res. Lett.* **2014**, *9*, 17.
(39) Kumar, M. S.; Rao, M. C. Effect of Al2O3 on Structural and Dielectric Properties of PVP-CH3COONa Based Solid Polymer Electrolyte Films for Energy Storage Devices. *Heliyon* **2019**, *5*, No. E02727.
(40) Zeng, Y.-X.; Zhong, X.-W.; Liu, Z.-Q.; Chen, S.; Li, N. Preparation and Enhancement of Thermal Conductivity of Heat Transfer Oil-Based MoS 2 Nanofluids. *J. Nanomater.* **2013**, *2013*, No. 3.
(41) Senthilkumar, S. R.; Sivakumar, T. Green Tea (Camellia Sinensis) Mediated Synthesis of Zinc Oxide (ZnO) Nanoparticles and Studies on Their Antimicrobial Activities. *Int. J. Pharm. Pharm. Sci.* **2014**, *6*, 461−465.
(42) Alias, S. S.; Ismail, A. B.; Mohamad, A. A. Effect of PH on ZnO Nanoparticle Properties Synthesized by Sol-Gel Centrifugation. *J. Alloys Compd.* **2010**, *499*, 231−237.
(43) Rahma, A.; Munir, M. M.; Khairurrijal; Prasetyo, A.; Suendo, V.; Rachmawati, H. Intermolecular Interactions and the Release Pattern of Electrospun Curcumin-Polyvinyl(Pyrrolidone) Fiber. *Biol. Pharm. Bull.* **2016**, *39*, 163−173.
(44) Lu, L.; Cai, J.; Frost, R. L. Desorption of Stearic Acid upon Surfactant Adsorbed Montmorillonite: AAA Thermogravimetric Study. *J. Therm. Anal. Calorim.* **2010**, *100*, 141−144.
(45) Peng, K.; Fu, L.; Li, X.; Ouyang, J.; Yang, H. Stearic Acid Modified Montmorillonite as Emerging Microcapsules for Thermal Energy Storage. *Appl. Clay Sci.* **2017**, *138*, 100−106.
(46) Sivaiah, K.; Kumar, K. N.; Naresh, V.; Buddhudu, S. Structural and Optical Properties of Li^+: PVP & Ag^+: PVP Polymer Films. *Mater. Sci. Appl.* **2011**, *02*, 1688−1696.
(47) Park, B. K.; Kim, D.; Jeong, S.; Moon, J.; Kim, J. S. Direct Writing of Copper Conductive Patterns by Ink-Jet Printing. *Thin Solid Films* **2007**, *515*, 7706−7711.
(48) Yang, Y.; Dong, H.; Wang, Y.; He, C.; Wang, Y.; Zhang, X. Synthesis of Octahedral like Cu-BTC Derivatives Derived from MOF Calcined under Different Atmosphere for Application in CO Oxidation. *J. Solid State Chem.* **2018**, *258*, 582−587.
(49) Strandwitz, N. C.; Nonoguchi, Y.; Boettcher, S. W.; Stucky, G. D. In Situ Photopolymerization of Pyrrole in Mesoporous TiO2. *Langmuir* **2010**, *26*, 5319−5322.
(50) Han, S.; Liu, K.; Hu, L.; Teng, F.; Yu, P.; Zhu, Y. Superior Adsorption and Regenerable Dye Adsorbent Based on Flower-Like Molybdenum Disulfide Nanostructure. *Sci. Rep.* **2017**, *7*, No. 43599.
(51) Salleh, M. A. M.; Mahmoud, D. K.; Karim, W. A. W. A.; Idris, A. Cationic and Anionic Dye Adsorption by Agricultural Solid Wastes: A Comprehensive Review. *Desalination.* **2011**, *280*, 1−13.
(52) Wang, S.; Liu, L. Fabrication of Novel Nanoporous Copper Powder Catalyst by Dealloying of ZrCuNiAl Amorphous Powders for the Application of Wastewater Treatments. *J. Hazard. Mater.* **2017**, *340*, 445−453.
(53) Guo, Y.; Zhou, C.; Fang, L.; Liu, Z.; Li, W.; Yang, M. Effect of PH on the Catalytic Degradation of Rhodamine B by Synthesized CDs/g-C3N4/Cu XO Composites. *ACS Omega* **2021**, *6*, 8119−8130.
(54) He, C.; Yang, J.; Zhu, L.; Zhang, Q.; Liao, W.; Liu, S.; Liao, Y.; Asi, M. A.; Shu, D. PH-Dependent Degradation of Acid Orange II by Zero-Valent Iron in Presence of Oxygen. *Sep. Purif. Technol.* **2013**, *117*, 59−68.
(55) Zhang, H.; Lv, X.; Li, Y.; Wang, Y.; Li, J. P25-Graphene Composite as a High Performance Photocatalyst. *ACS Nano* **2010**, *4*, 380−386.
(56) Üstün, G. E.; Solmaz, S. K. A.; Morsünbül, T.; Azak, H. S. Advanced Oxidation and Mineralization of 3-Indole Butyric Acid (IBA) by Fenton and Fenton-like Processes. *J. Hazard. Mater.* **2010**, *180*, 508−513.
(57) Djellabi, R.; Ghorab, M. F.; Sehili, T. Simultaneous Removal of Methylene Blue and Hexavalent Chromium From Water Using TiO 2 /Fe(III)/H 2 O 2 /Sunlight. CLEAN - Soil, Air. *Water* **2017**, *45*, No. 1500379.
(58) Sable, S. S.; Ghute, P. P.; Álvarez, P.; Beltrán, F. J.; Medina, F.; Contreras, S. FeOOH and Derived Phases: Efficient Heterogeneous Catalysts for Clofibric Acid Degradation by Advanced Oxidation Processes (AOPs). *Catal. Today* **2015**, *240*, 46−54.
(59) Özdemir, C.; Öden, M. K.; Şahinkaya, S.; Kalipçi, E. Color Removal from Synthetic Textile Wastewater by Sono-Fenton Process. *Clean: Soil, Air, Water* **2011**, *39*, 60−67.
(60) Sun, S.; Zhang, X.; Zhang, J.; Wang, L.; Song, X.; Yang, Z. Surfactant-Free CuO Mesocrystals with Controllable Dimensions: Green Ordered-Aggregation-Driven Synthesis, Formation Mechanism and Their Photochemical Performances. *CrystEngComm* **2013**, *15*, 867−877.
(61) Dong, C.; Zhong, M.; Huang, T.; Ma, M.; Wortmann, D.; Brajdic, M.; Kelbassa, I. Photodegradation of Methyl Orange under Visible Light by Micro-Nano Hierarchical Cu 2O Structure Fabricated by Hybrid Laser Processing and Chemical Dealloying. *ACS Appl. Mater. Interfaces* **2011**, *3*, 4332−4338.
(62) Djellabi, R.; Fouzi Ghorab, M.; Smara, A.; Bianchi, C. L.; Cerrato, G.; Zhao, X.; Yang, B. Titania−Montmorillonite for the Photocatalytic Removal of Contaminants from Water: Adsorb & Shuttle Process. In *Green Materials for Wastewater Treatment*; Springer, 2020; Vol. *38*, pp 291−319.
(63) Huang, H.; Guo, T.; Wang, K.; Li, Y.; Zhang, G. Efficient Activation of Persulfate by a Magnetic Recyclable Rape Straw Biochar Catalyst for the Degradation of Tetracycline Hydrochloride in Water. *Sci. Total Environ.* **2021**, *758*, No. 143957.
(64) Guo, T.; Jiang, L.; Wang, K.; Li, Y.; Huang, H.; Wu, X.; Zhang, G. Efficient Persulfate Activation by Hematite Nanocrystals for Degradation of Organic Pollutants under Visible Light Irradiation: Facet-Dependent Catalytic Performance and Degradation Mechanism. *Appl. Catal., B* **2021**, *286*, No. 119883.
(65) Tahmasebi, N.; Sezari, S.; Zaman, P. Fabrication and Characterization of Hydrogen-Treated Tungsten Oxide Nanofibers for Cationic Dyes Removal from Water. *Solid State Sci.* **2020**, *100*, No. 106073.
(66) Guo, T.; Wang, K.; Zhang, G.; Wu, X. A Novel α-Fe 2 O 3 @g-C 3 N 4 Catalyst: Synthesis Derived from Fe-Based MOF and Its Superior Photo-Fenton Performance. *Appl. Surf. Sci.* **2019**, *469*, 331−339.
(67) Gomathi Devi, L.; Girish Kumar, S.; Mohan Reddy, K.; Munikrishnappa, C. Photo Degradation of Methyl Orange an Azo Dye by Advanced Fenton Process Using Zero Valent Metallic Iron: Influence of Various Reaction Parameters and Its Degradation Mechanism. *J. Hazard. Mater.* **2009**, *164*, 459−467.

https://doi.org/10.1021/acsomega.1c02881
ACS Omega 2021, 6, 22188−22201

(68) Fathima, N. N.; Aravindhan, R.; Rao, J. R.; Nair, B. U. Dye House Wastewater Treatment through Advanced Oxidation Process Using Cu-Exchanged Y Zeolite: A Heterogeneous Catalytic Approach. *Chemosphere* **2008**, *70*, 1146−1151.
(69) Taran, O. P.; Zagoruiko, A. N.; Ayusheev, A. B.; Yashnik, S. A.; Prihod'ko, R. V.; Ismagilov, Z. R.; Goncharuk, V. V.; Parmon, V. N. Wet Peroxide Oxidation of Phenol over Cu-ZSM-5 Catalyst in a Flow Reactor. Kinetics and Diffusion Study. *Chem. Eng. J.* **2015**, *282*, 108−115.

https://doi.org/10.1021/acsomega.1c02881
ACS Omega 2021, 6, 22188−22201